*J. Fluid Mech.* (1982), *vol.* 117, *pp.* 379–402
*Printed in Great Britain*



# Transport near a vertical ice surface melting in saline water: some numerical calculations

By VAN P. CAREY

Department of Mechanical and Aerospace Engineering,
State University of New York at Buffalo, Amherst, NY 14260, U.S.A.

AND BENJAMIN GEBHART

Department of Mechanical Engineering and Applied Mechanics,
University of Pennsylvania, Philadelphia, PA 19104, U.S.A.

(Received 14 January 1981)

Computed numerical results are presented for the laminar buoyancy-induced flows driven by combined thermal and saline transport near a vertical melting ice surface in saline water. Results are presented which indicate that conventional boundary-layer flow occurs for some combinations of ambient salinity and temperature in the ranges 0 to 31‰ and −1 to 20 °C, respectively. These conditions are very common in terrestrial waters. The analysis used herein is the first to model fully the many complicated aspects of these flows. The present analysis includes simultaneous transport of salt and thermal energy as well as the effect of interface motion. The formulation uses the most recently available transport properties and a very accurate equation of state for the density of pure and saline water. The interface temperature and salinity, which are not known *a priori*, are here determined jointly from the transport equations, and from species-conservation and phase-equilibrium relations at the ice surface. At low ambient temperatures, the flow is found to be dominated by the upward saline buoyancy, resulting in upward flow. However, at high temperatures and low salinities, the downward thermal buoyancy overcomes the upward saline buoyancy near the surface to cause downward flow. For choices of ambient conditions between these extremes, the opposing saline and thermal buoyancy are about equal in strength. The resulting tendency for bi-directional flow at these intermediate circumstances caused numerical stability problems which made it impossible to obtain convergent solutions for some cases. However, calculated solutions were obtained at ambient salinities below 5‰, for ambient temperatures between 8 and 20 °C, and at temperatures below 4 °C, for ambient salinities between 0 and 31‰. These solutions indicate the limits of the range of conditions for which laminar boundary layer flow occurs. They further suggest that outside these ranges, the flow may be laminar and bi-directional. The very strong buoyancy which characterizes some of these conditions suggests that they may become turbulent at short downstream distances. The computed results are seen to be in excellent agreement with the limited experimental data and observations of previous studies.

## 1. Introduction

Recent interest in the melting of ice masses in saline water has stemmed from efforts to understand better the mechanisms that affect the size of the polar ice pack, the deterioration of icebergs in shipping lanes, and the melting of glaciers in fjords. The transport near a vertical ice surface melting in quiescent sea water is of particular interest, since it relates to the melting of pack ice and icebergs in the polar regions. Although melting does occur along the bottom of ice masses floating in warmer sea water, the melting of the vertical surfaces has been observed to contribute most to the total melt rate. Neshyba & Josberger (1980) have estimated that the ratio of side-wall to bottom melt rate for icebergs is of the order of 33 to 1. Knowledge of the flow and transport along the side surface of the ice mass is therefore essential to accurately predict iceberg melting rates.

The flow and transport adjacent to a vertical ice surface melting into quiescent water at oceanic salinities has been the subject of several investigations. Marschall (1977) reports the solution of the boundary-layer equations governing heat, mass and momentum transfer near a vertical ice surface melting in saline water. He used a co-ordinate system fixed to the ice–water interface and derived an expression for the blowing velocity at the ice surface resulting from the melting. He apparently used the additional condition of conservation of salt at the interface, along with the transport equations, to determine the interface salinity. Marschall (1977) reports that the governing equations and boundary conditions admit a similarity solution, but gives no details about the method of calculation or the resulting flow and transport. However, the computed interface salinity and temperature conditions as a function of ambient temperature $t_\infty$ are presented for an ambient salinity, $s_\infty$ of 35‰.

In a later study, Johnson (1978) measured the ice melting rates for a vertical ice surface melting in quiescent saline water at various ambient temperatures for an ambient salinity of 35‰. Schlieren photographs were taken of the flow field near the ice surface. The net flow was found to be upward for $-0{\cdot}7\ ^\circ\mathrm{C} \leqslant t_\infty \leqslant 20{\cdot}7\ ^\circ\mathrm{C}$. The flow was observed to be laminar near the lower edge and turbulent over the upper portion of the surface. The length of the laminar region as well as the interface salinity $s_0$ was found to depend on $t_\infty$. The effect of ambient stratification on the flow and transport adjacent to a vertical ice surface melting in saline water has also been studied experimentally by Huppert & Turner (1978).

Gebhart & Mollendorf (1978) have derived similarity equations governing the buoyancy-driven flow adjacent to a vertical impermiable surface in cold water with simultaneous transport of salt and thermal energy. They discussed the necessary conditions for similarity and the application of the equations to freezing and melting circumstances, but presented no calculations.

The most extensive examination, to date, of the flow near a melting vertical ice surface in saline water is the recent study of Josberger & Martin (1981). Using illuminated particles and dye injection, they observed the flow behaviour near the ice surface for ambient salinities near 33‰, at ambient water temperatures ranging from $-1{\cdot}15$ to 26 °C. They found that for $t_\infty$ less than about 18 °C, the flow near the surface was laminar and bi-directional near the bottom, while fully upward, turbulent flow

was found near the top. At the vertical location $l$ above the bottom edge, the entrainment toward the surface splits, with the upper part feeding the turbulent upflow and the lower part feeding the laminar bi-directional flow. This splitting entrainment, which resembles an impinging jet, produces a high local melt rate. As $t_\infty$ increased, $l$ generally decreased. The lower bi-directional and upper turbulent flow were studied separately, measuring the surface temperature distribution and the ice melting rate for each over a range of ambient conditions. In the lower bi-directional flow, the measured temperature was not uniform along the ice surface, whereas the vertical turbulent flow produced uniform surface conditions. An eddy-viscosity model was used to compute the behaviour of the upward turbulent flow. As $t_\infty$ was increased from about 18 °C to about 23 °C, flow 'inversion' occurred. Josberger & Martin (1981) found that at 23 °C the flow near the top of the ice was laminar and bi-directional, and near the lower portion of the surface the flow was turbulent and fully downward. At lower salinities, $(t_\infty, s_\infty) = (0{\cdot}05, 14{\cdot}2)$ and $(1{\cdot}80, 8{\cdot}0)$, Josberger & Martin (1981) observed fully upward laminar flow and uniform wall temperatures. A detailed discussion of the correlation between these experimental results and field observations of icebergs may be found in Josberger (1979).

The studies described above have concentrated primarily on ice melting at oceanic salinities, near 35‰. Studies by Vanier & Tien (1968), Gebhart & Mollendorf (1978), Carey, Gebhart & Mollendorf (1980), Wilson & Vyas (1979), and Carey & Gebhart (1981) have established the flow behaviour near a vertical ice surface melting in pure water at low temperatures. These latter circumstances are obviously related to transport processes near melting ice masses in fresh-water lakes and rivers. The intermediate range of salinities, between 0 and 35‰ can also arise in the environment and in technological applications. For example, where rivers empty into the ocean, the mixing of fresh and saline waters can result in local salinities in this range. Likewise, near discharge pipes saline contaminants present in sewage or industrial wastes may raise the salinity of the water locally. Consequently, ice melting in weakly saline or brackish water is also important. The objective of the present study was to obtain more complete information regarding the flow and transport near a melting vertical ice surface at these intermediate salinities.

At oceanic salinities, the transport near a melting vertical ice surface is complicated by a number of factors. The thermal and saline buoyancy forces are opposed. The Schmidt number $Sc$ is large ($\simeq 3000$) while the Prandtl number $Pr$ is smaller ($\simeq 10$). Consequently, in laminar flow, the very large saline buoyancy force is confined to a small saline boundary layer near the surface, while the smaller thermal buoyancy force is dominant further from the surface. It will be shown here that the interface-motion effects cannot be neglected in these flows. In water at lower salinities all these factors are still present and, in addition, the transport is further complicated by the presence of a density extremum at low temperatures.

The complicating factors noted above make analysis of the resulting transport very difficult. The previous studies of these flows have been largely experimental. Marschall (1977) outlined an analysis, but presented only the resulting interface conditions for $s_\infty = 35‰$. The results of Josberger & Martin (1981) indicate that conventional boundary-layer flow does not occur for these circumstances. This casts doubt on the validity of Marschall's (1977) results, which are based on boundary-layer theory. Josberger & Martin (1981) present the computed results of an eddy-diffusivity model

of the turbulent upflow observed at oceanic salinities for $-2\ °C < t_\infty < 18\ °C$. Evaluation of the coefficients in their model was based on their experimental measurements.

While the experiments of Josberger & Martin (1981) indicate very complicated flow behaviour at salinities near 35‰, at lower salinities conventional boundary layer flow may result. In the present study, a modified form of the formulation of Gebhart & Mollendorf (1978), has been used to compute the boundary-layer flow and transport adjacent to a melting vertical ice surface in saline water. Calculations were attempted over the full range of ambient salinities from 0 to 35‰. However, numerically computed results were obtained only for some combinations of ambient salinity and temperature in the ranges 0 to 31‰ and $-1$ to 20 °C, respectively. The experimental observations of Josberger & Martin (1981) and those of Carey & Gebhart (1981) indicate that for some combinations of $t_\infty$ and $s_\infty$ in these ranges the flow departs strongly from conventional boundary-layer behaviour. For these non-conventional circumstances, computed results were not obtained. However, the computed results represent an extensive portion of these ranges and they indicate the conditions at which transition to non-boundary-layer flow occurs. In a companion paper, Carey & Gebhart (1982), it will be shown that the computed results are in good agreement with experimental measurements.

In the present analysis, the transport property data compiled by Mollendorf, Kukulka & Gebhart (1982) and the very accurate density relation of Gebhart & Mollendorf (1977) were used. Interface-motion effects were included and the interface salinity and temperature were determined from the computed transport using an iterative procedure. The computed interface conditions and transport parameters are presented for conditions resulting in fully upward, fully downward and bi-directional flow. Representative velocity, temperature and buoyancy-force profiles are also presented for each of these flow regions. The results of these computations, when combined with the experimental observations of Josberger & Martin (1981) and those of Carey & Gebhart (1982) indicate the different regimes of flow behaviour that result for $0‰ \leqslant s_\infty \leqslant 35‰$, $-1\ °C \leqslant t_\infty \leqslant 20\ °C$.

## 2. Analysis

The present analysis assumes constant absolute viscosity $\mu$, thermal conductivity $k$, salt diffusivity $D$, and specific heat $c_p$. The salt concentration $s$ is assumed to be small compared with the density of water. The Sorét and Dufour effects are small and will be neglected. The $x$-direction is first taken positive in the direction opposed to gravity, i.e. $\mathbf{g} = -g\mathbf{i}$, where $\mathbf{i}$ is the unit vector in the $x$-direction. The $y$-direction is taken normal to the ice surface. With the co-ordinate system taken as stationary relative to the far ambient medium, the ice–water interface moves in the negative $y$-direction with velocity $V_i(x)$ as the ice melts. Thus, in this reference frame, the flow field is time-dependent. It can be easily shown from order-of-magnitude arguments that this time dependence has an effect $O(1)$ even at low ambient water temperatures which result in low melting rates. In this regard, flows near ice melting in saline water are unlike those in pure water, where interface-motion effects may be neglected at low ambient temperatures with little loss in accuracy. A more detailed discussion of these matters may be found in Carey (1981). As for Boussinesq flows, the variation of density is neglected, except for the buoyancy-force term. Pressure work and viscous

dissipation are also neglected in the energy equation. Assuming two-dimensional, boundary-layer flow, mostly in the $x$-direction, the time-dependent governing equations are

$$\frac{\partial u}{\partial x}+\frac{\partial v}{\partial y}=0, \tag{1}$$

$$\rho_1\left(\frac{\partial u}{\partial \tau}+u\frac{\partial u}{\partial x}+v\frac{\partial u}{\partial y}\right)=\mu\frac{\partial^2 u}{\partial y^2}+g(\rho_\infty-\rho), \tag{2}$$

$$\rho_1 c_p\left(\frac{\partial t}{\partial \tau}+u\frac{\partial t}{\partial x}+v\frac{\partial t}{\partial y}\right)=k\frac{\partial^2 t}{\partial y^2}, \tag{3}$$

$$\frac{\partial s}{\partial \tau}+u\frac{\partial s}{\partial x}+v\frac{\partial s}{\partial y}=D\frac{\partial^2 s}{\partial y^2}. \tag{4}$$

The change in density accompanying the phase change causes the ambient fluid to move toward the ice surface with a velocity $V_a$. Since $V_a(x)$ and the interface velocity $V_i(x)$ are both determined by the melt rate they are related to each other as

$$V_a(x)=V_i(x)\left\{1-\frac{\rho_i}{\rho_1(1-\frac{1}{1000}s_0)}\right\}, \tag{5}$$

where the salinity $s$ is in parts per thousand (‰), and $s_0$ is the salinity at the interface. As discussed in § 1, for laminar boundary-layer flow adjacent to a vertical ice surface melting in saline water, the measurements of Josberger & Martin (1981) indicate that the temperature is uniform along the ice surface. Hence it is assumed here that $t_0$ and $s_0$ are constant along the ice surface. Assuming also that $V_i$ is independent of time and that the entire ice mass is at the uniform temperature $t_0$, the boundary conditions are

$$u=0, \quad v=-V_a, \quad t=t_0, \quad s=s_0 \quad \text{at} \quad y=-V_i\tau; \tag{6a}$$

$$u=0, \quad t=t_\infty, \quad s=s_\infty \quad \text{at} \quad y\to\infty. \tag{6b}$$

The equations and boundary conditions are now transformed to a co-ordinate system with the $\bar{x}$-axis along the ice interface and moving with it. The following transformation is used:

$$x=\bar{x}, \quad y=\bar{y}-V_i\bar{\tau}, \quad \tau=\bar{\tau}; \tag{7a}$$

$$u=\bar{u}, \quad v=\bar{v}-V_i, \quad t=\bar{t}, \quad s=\bar{s}. \tag{7b}$$

In addition to the previous assumption that $V_i$ is independent of time, it is further assumed that in the co-ordinate system moving with the interface, the flow field is independent of time and that $V_i^{-1}(dV_i/dx)$ is small and may be neglected. These assumptions are valid for a vertical ice surface melting in saline water as long as the melting does not cause the surface geometry to deviate greatly from its initially flat vertical configuration. For the boundary-layer flow considered here, this will be true away from the leading edge. Using the above assumptions and the transformations in (7*a*, *b*), the governing equations (1)–(4) become

$$\frac{\partial \bar{u}}{\partial \bar{x}}+\frac{\partial \bar{v}}{\partial \bar{y}}=0, \tag{8}$$

$$\rho_1\left(\bar{u}\frac{\partial \bar{u}}{\partial \bar{x}}+\bar{v}\frac{\partial \bar{u}}{\partial \bar{y}}\right)=\mu\frac{\partial^2 \bar{u}}{\partial \bar{y}^2}+g(\rho_\infty-\rho), \tag{9}$$

$$\rho_1 c_p \left(\bar{u}\frac{\partial \bar{t}}{\partial \bar{x}} + \bar{v}\frac{\partial \bar{t}}{\partial \bar{y}}\right) = k\frac{\partial^2 \bar{t}}{\partial \bar{y}^2}, \tag{10}$$

$$\bar{u}\frac{\partial \bar{s}}{\partial \bar{x}} + \bar{v}\frac{\partial \bar{s}}{\partial \bar{y}} = D\frac{\partial^2 \bar{s}}{\partial \bar{y}^2}. \tag{11}$$

At the interface, fluid now appears to be generated at the ice surface by the melting process with a velocity $V_0(x)$ normal to the surface. From conservation of mass and thermal energy at the interface, and including the effect of density change, it is possible to relate $V_0$ to the temperature gradient at the surface as follows:

$$V_0 = V_1\left(\frac{\rho_1}{\rho_1(1-\frac{1}{1000}s_0)}\right) = \frac{k}{\rho_1(1-\frac{1}{1000}s_0)\,h_{11}}\left(\frac{\partial \bar{t}}{\partial \bar{y}}\right)_{\bar{y}=0}, \tag{12}$$

where $\rho_1$ is the fluid density at some reference condition and $h_{11}$ is the latent heat of fusion for ice. After transforming, the boundary conditions for (8)–(11) become

$$\bar{u} = 0, \quad \bar{v} = V_0, \quad \bar{t} = t_0, \quad \bar{s} = s_0 \quad \text{at} \quad \bar{y} = 0, \tag{13}$$

$$\bar{u} = 0, \quad \bar{t} = t_\infty, \quad \bar{s} = s_\infty \quad \text{at} \quad \bar{y} \to \infty. \tag{14}$$

Conservation of salt and water as separate species at the interface also requires

$$\frac{ks_0}{h_{11}}\left(\frac{\partial \bar{t}}{\partial \bar{y}}\right)_{\bar{y}=0} - \tfrac{1}{1000}(1000 - s_0)\,D\rho_1\left(\frac{\partial \bar{s}}{\partial \bar{y}}\right)_{\bar{y}=0} = 0. \tag{15}$$

As will be seen later, this condition will be used to determine the unknown interface conditions.

Following Gebhart & Mollendorf (1978), a similarity variable $\eta(\bar{x}, \bar{y})$, stream functions $\psi(\bar{x}, \bar{y})$ and $f(\eta)$, and temperature and salinity functions are defined as

$$\eta = \bar{y}b(\bar{x}), \quad \psi = \nu c(\bar{x}) f(\eta), \tag{16}$$

$$\phi = (\bar{t} - t_\infty)/(t_0 - t_\infty), \quad S = (\bar{s} - s_\infty)/(s_0 - s_\infty), \tag{17}$$

$$c(\bar{x}) = 4(\tfrac{1}{4}Gr_{\bar{x}})^{\frac{1}{4}} = G, \quad b = G/4\bar{x}. \tag{18}$$

Here $t_0$, $t_\infty$, $s_0$ and $s_\infty$ are taken as constant, with $t_0$ and $s_0$ initially unknown. The definition of the Grashof number $Gr_{\bar{x}}$ is discussed later in this section.

The simple '$n = 2$' form of the density correlation of Gebhart & Mollendorf (1977) is used to evaluate the buoyancy term in (9). This form of their correlation has only linear terms in salinity. The correlation is given by

$$\rho(t, s, p) = \rho_m(s, p)\{1 - \alpha(s, p)\,|t - t_m(s, p)|^q\}, \tag{19}$$

$$\rho_m(s, p) = \rho_m(0, 1)\{1 + f_1(p) + sg_1(p)\}, \tag{20a}$$

$$\alpha(s, p) = \alpha(0, 1)\{1 + f_2(p) + sg_2(p)\}, \tag{20b}$$

$$t_m(s, p) = t_m(0, 1)\{1 + f_3(p) + sg_3(p)\}, \tag{20c}$$

$$f_i(p) = f_{i1}(p - 1) + f_{i2}(p - 1)^2, \tag{20d}$$

$$g_i(p) = g_{i0} + g_{i1}(p - 1) + g_{i2}(p - 1)^2, \tag{20e}$$

where $q = 1{\cdot}894816$, $\rho_m(0, 1) = 999{\cdot}9720$ kg m$^{-3}$, $\alpha(0, 1) = 9{\cdot}297173 \times 10^{-6}$ (°C)$^{-q}$, $t_m(0, 1) = 4{\cdot}029325$ °C, and $s$ and $p$ are in ‰ and bars respectively. The constants $f_{ij}$

and $g_{ij}$ are given in Gebhart & Mollendorf (1977). Gebhart & Mollendorf (1977) applied a regression analysis to the most recent density data for saline water to determine the constants in the density correlation to seven significant figures. This level of precision was retained here to incorporate the full accuracy of the density correlation in the buoyancy force term.

Substituting (16)–(20), the density difference in (9) becomes

$$\frac{\rho_\infty - \rho}{\rho_m(s_\infty, p)\,\alpha(s_\infty, p)\,|t_0 - t_\infty|^a} = \{1 + AS\}\{1 + BS\}\,|\phi - R - QS|^a - |R|^a - PS, \tag{21}$$

where

$$R = \{t_m(s_\infty, p) - t_\infty\}/(t_0 - t_\infty), \tag{22a}$$

$$A = g_1(p)\,(s_0 - s_\infty)\,\rho_m(0, 1)/\rho_m(s_\infty, p), \tag{22b}$$

$$B = g_2(p)\,(s_0 - s_\infty)\,\alpha(0, 1)/\alpha(s_\infty, p), \tag{22c}$$

$$Q = g_3(p)\,(s_0 - s_\infty)\,t_m(0, 1)/(t_0 - t_\infty), \tag{22d}$$

$$P = g_1(p)\,(s_0 - s_\infty)\,\rho_m(0, 1)/\alpha(s_\infty, p)\,\rho_m(s_\infty, p)\,|t_0 - t_\infty|^a. \tag{22e}$$

For convenience, $\rho_1$ is taken equal to $\rho_m(s_\infty, p)$. With $t_0$ and $s_0$ constant, similarity is obtained, and the governing equations become

$$f''' + 3ff'' - 2f'^2 + W = 0, \tag{23a}$$

$$\phi'' + 3Prf\phi' = 0, \tag{23b}$$

$$S'' + 3Scf S' = 0, \tag{23c}$$

where $W$ in (23$a$) is related to $\rho_\infty - \rho$ and the definition of $Gr_{\bar{x}}$. This formulation permits some variation in the definitions of $Gr_{\bar{x}}$ and the buoyancy force $W$. The numerical scheme used to calculate solutions of (23) was found to be most stable when $Gr_{\bar{x}}$ was defined so that $W$ is $O(1)$ and when $\bar{x}$ is taken to be positive in the direction of net mass flow. At low temperatures, below about 5 °C, the flow is upward and dominated by the strong upward saline buoyancy force. Therefore, $\bar{x}$ is taken positive in the vertically upward direction and $W$ and $Gr_{\bar{x}}$ are defined as

$$W = -\frac{1}{P}\{(1 + AS)\,(1 + BS)\,|\phi - R - QS|^a - |R|^a - PS\}, \tag{24a}$$

$$Gr_{\bar{x}} = (-P)\frac{g\alpha(s_\infty, p)\,\bar{x}^3|t_0 - t_\infty|^a}{\nu^2} = \frac{\rho_m(0, 1)}{\rho_m(s_\infty, p)}\frac{g g_1(p)\,\bar{x}^3(s_\infty - s_0)}{\nu^2}. \tag{24b}$$

At higher temperatures, above about 5 °C, the flow is mostly downward and is dominated by the downward thermal buoyancy force. At high temperatures, $\bar{x}$ is therefore taken to be positive-downward and $Gr_{\bar{x}}$ and $W$ are defined as

$$W = PS + |R|^a - (1 + AS)\,(1 + BS)\,|\phi - R - QS|^a, \tag{25a}$$

$$Gr_{\bar{x}} = \frac{g\alpha(s_\infty, p)\,\bar{x}^3|t_0 - t_\infty|^a}{\nu^2}. \tag{25b}$$

At intermediate temperatures, near about 5 °C, it is not clear, *a priori*, which net flow direction results and which formulation, (24) or (25), applies. The range of ambient conditions that correspond to each formulation were determined by trial and error.

The additional parameters that have arisen in $W$, owing to saline diffusion, are $A$, $B$, $Q$ and $P$. The magnitudes of $A$ and $B$ are usually small compared with 1. They represent the effects of the local salinity level on the levels of $\rho_m$ and $\alpha$. $PS$ is the principal component of the contribution of the salinity gradient to the buoyancy force. From (22$e$) it is seen that this is a very large term for $s_0 - s_\infty$ large and $t_0 - t_\infty$ small. This gives a large effect on $\rho_\infty - \rho$ compared with the temperature effect. However, since $Sc$ is large, the salinity diffusion layer is very thin. The other salinity contribution $Q$ is the effect of local salinity on $t_m$. Although the term $QS$ may be larger than $\phi$ for $s_0 - s_\infty$ large, its range of effect, in $\eta$, is small.

With the similarity transformation, the boundary conditions (13) and (14) become

$$f(0) = \frac{-\phi'(0)\, c_p(t_0 - t_\infty)}{3h_{11} Pr(1 - 10^{-3}s_0)}, \quad f'(0) = 0, \quad \phi(0) = 1, \quad S(0) = 1; \tag{26a}$$

$$f'(\infty) = \phi(\infty) = S(\infty) = 0; \tag{26b}$$

and the expression for conservation of species at the interface (15) becomes

$$\frac{S'(0)}{\phi'(0)} - \frac{Sc}{Pr}\frac{c_p(t_0 - t_\infty)}{h_{11}} \frac{s_0}{(1 - 10^{-3}s_0)(s_0 - s_\infty)} = 0. \tag{27}$$

The basic transport quantities as seen from a co-ordinate system fixed relative to the far ambient medium, in terms of similarity variables, are

$$u = \nu c b f'(\eta) = \nu \frac{G^2}{4x} f'(\eta), \tag{28a}$$

$$-v = \frac{\nu G}{4x}\left\{3f - 3\frac{\rho_1}{\rho_i}(1 - 10^{-3}s_0) f(0) - \eta f'\right\}, \tag{28b}$$

$$\sigma(x) = \frac{\mu \nu G^3}{16x^2} f''(0), \tag{28c}$$

$$Nu_x = \frac{h_x x}{k} = -\sqrt{\tfrac{1}{2}}\, \phi'(0) Gr_x^{\frac{1}{4}}, \tag{28d}$$

$$Sh_x = \frac{h_{D,x} x}{\rho_1 D} = -\sqrt{\tfrac{1}{2}}\, S'(0) Gr_x^{\frac{1}{4}}, \tag{28e}$$

where $h_x$ and $h_{D,x}$ are the local heat- and mass-transfer coefficients respectively, $\sigma(x)$ is the local surface shear stress, $Nu_x$ is the local Nusselt number and $Sh_x$ is the local Sherwood number. Here, $\eta$ is evaluated at $\bar{y}$, $\eta = \bar{y} b(x)$, where $\bar{y} = y + V_1 \tau$ is the instantaneous horizontal distance between the position of interest in the flow and the ice surface. Another quantity of interest is the integral of the buoyancy force

$$I_W = \int_0^\infty W(\eta)\, d\eta,$$

where $W$ is given by (24$a$) or (25$a$).

Note that from condition (12), the $x$-variation of $V_0$ is the same as that of the surface heat flux. For the isothermal condition here, the heat flux, and therefore $V_0$, are proportional to $x^{-\frac{1}{4}}$. Fortunately, this is the exact $x$-dependence required to preserve similarity in the boundary condition for $f(0)$. Hence the effect of interface motion is included without spoiling similarity.

If local thermodynamic equilibrium is assumed, $t_0$ will equal the equilibrium ice-melting temperature at the interface salinity $s_0$. Using the relation determined by Fujino, Lewis & Perkin (1974),

$$t_{il}(s,p) = -0{\cdot}02831 - 0{\cdot}0499s - 0{\cdot}000112s^2 - 0{\cdot}00759p, \tag{29a}$$

where $t_{il}$ is the equilibrium ice-melting temperature and $s$ and $p$ are respectively in ‰ and bars, yields $t_0 = t_{il}(s_0)$. The relation of Fujino *et al.* (1974) is in good agreement with measured data down to at least 4‰ salinity. However, for $p = 1$ it is in error very close to $s = 0$. Therefore, for $p = 1$, (29*a*) was used down to $s_0 = 2$‰. The following simple linear relation was used below 2‰:

$$t_{il}(s,1) = -0{\cdot}06807s \quad (p = 1, s < 2) \tag{29b}$$

This form agrees with (29*a*) at $s = 2$ and goes linearly to 0 as $s$ goes to zero. Since $t_0 = t_{il}(s_0)$, (27) together with (29*a*) and (29*b*) provide a relation between $s_0$ and the transport parameters $\phi'(0)$ and $S'(0)$.

The transport equations (23) with boundary conditions (26) and either (24*a*) or (25*a*) must therefore be solved while simultaneously satisfying (27). The computational scheme is described in § 3.

## 3. Calculations

Using either (24*a*) or (25*b*), (23) with boundary conditions (26) were integrated using a predictor–corrector shooting method. This scheme included automatic local subdivision of step size to maintain accuracy, while integrating from $\eta = 0$ to $\eta = \eta_{\text{edge}}$. Initially unknown values of $\phi'(0)$, $S'(0)$ and $f''(0)$ were guessed and subsequently corrected to satisfy the far-boundary conditions. The step size, the accuracy criterion, and the value of $\eta_{\text{edge}}$ were adjusted to obtain values of $f''(0)$, $S'(0)$, $\phi'(0)$ and $f(\infty)$ unchanging to five digits.

The integration procedure described above was only part of the full computational procedure. The complete program ran as follows. First, a value of $s_0$ was guessed. Using (29*a*) or (29*b*), $t_0$ was computed, and from $s_0$, $s_\infty$, $t_0$ and $t_\infty$ the film conditions, $s_f = \frac{1}{2}(s_0 + s_\infty)$ and $t_f = \frac{1}{2}(t_0 + t_\infty)$, were calculated. At $t_f$ and $s_f$, $Pr$, $Sc$ and $c_p$ were calculated by interpolating the tabulated results of Mollendorf *et al.* (1982). Again using $t_0$, $t_\infty$, $s_0$ and $s_\infty$, (19), (20) and (22) were used to compute $A$, $B$, $Q$, $R$ and $P$. Then, the governing equations (23) with boundary conditions (26) were integrated to convergence as described above. At this stage, convergence to the value of $s_0$ satisfying (27) was checked. If (27) was not satisfied, a new value of $s_0$ was computed using a Newton–Raphson scheme and the program iterated again. When (27) was satisfied such that the value of $s_0$ was determined to four significant figures, the program terminated.

Computations here were done only for $p = 1$ bar, although the formulation permits computations at any pressure level from 1 to 1000 bars. At $p = 1$ bar, $f_i(p) = 0$ and $g_i(p) = g_{i0}$, where the $g_{i0}$ are the constants

$$g_{10} = 8{\cdot}046157 \times 10^{-4}, \quad g_{20} = -2{\cdot}839092 \times 10^{-3}, \quad g_{30} = -5{\cdot}265509 \times 10^{-2}. \tag{30}$$

The Prandtl and Schmidt numbers are strongly temperature-dependent, but weakly dependent on salinity. Calculation of $Pr$ and $Sc$ at $t_f$ was accomplished by fitting

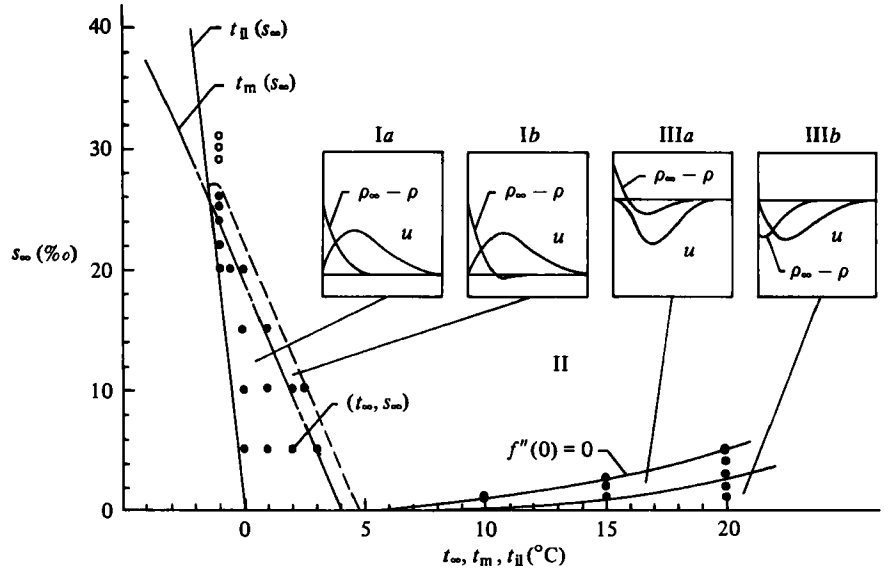


FIGURE 1. Flow regimes and buoyancy-force distributions corresponding to different regions of the $(t_\infty, s_\infty)$-plane. The circles indicate points at which full (●) or asymptotic (○) solutions were calculated.

fourth-degree Lagrange interpolating polynomials to the tabulated data of Mollendorf *et al.* (1982). The value of $Pr$ at $t_f$ and $s_f$ was determined by computing $Pr$ at $t_f$ for $s = 0$ and $s = 20‰$, and then linearly interpolating to get $Pr$ at $s_f$. The only available data for $Sc$ which included the temperature dependence was that at $s = 28‰$. Since the salinity dependence is weak, the value of $Sc$ at $t_f$ and $s = 28‰$ was used. There is not sufficient data available to interpolate for the value at $s_f$. The specific heat $c_p$ is only weakly dependent on both temperature and salinity. Therefore, $c_p$ was computed at $t_f$ and $s_f$ by linearly interpolating the tabulated values of Mollendorf *et al.* (1982). The polynomials for $Pr$ and $Sc$ and the $c_p$ data used here may be found in Carey (1981). The latent heat of melting for ice was taken to be constant, $h_{ll} = 79{\cdot}77$ cal/g.

Owing to limitations on the density correlation, the formulation is limited to ambient salinities less than $40‰$ and ambient temperatures less than 20 °C. Assuming local thermodynamic equilibrium, melting occurs only when the ambient temperature is greater than the equilibrium melting temperature at the chosen ambient salinity, i.e. $t_\infty \geqslant t_{ll}(s_\infty)$. Computation of the transport and interface condition was attempted over the entire range, but, as will be discussed in § 4, convergent solutions were obtained only in certain ranges of $t_\infty$ and $s_\infty$.

## 4. Results

The range of ambient-medium conditions for which convergent solutions were obtained is shown in figure 1. A black dot marks the $(t_\infty, s_\infty)$-co-ordinates of each of the computed solutions. Also noted are the different flow regimes corresponding to different regions of the $(t_\infty, s_\infty)$-plane. Assuming local thermodynamic equilibrium, melting occurs for $t_\infty > t_{ll}(s_\infty)$. Therefore, all points considered here are to the right

of the $t_{11}(s_\infty)$ line in figure 1. For values of $t_\infty$ to the left of the $t_m(s_\infty)$ line, the thermal buoyancy acts completely upward. Therefore, as shown in figure 1, in region I$a$, the saline and thermal buoyancy both act to drive the flow up. The net buoyancy force $\rho_\infty - \rho$ is positive everywhere in the thermal- and saline-transport regions. For choices of $t_\infty$ and $s_\infty$ in region I$b$, slightly to the right of the $t_m(s_\infty)$ line, the thermal-buoyancy effect is locally bi-directional. Whereas the saline buoyancy acts entirely upward, the buoyancy due to the temperature field acts up near the surface and down near the outer edge of the thermal boundary layer. Characteristic buoyancy force and velocity profiles for region I$b$ are shown in figure 1. Computed results have been obtained in regions I$a$ and I$b$. In region I$a$, the fully-upward buoyancy force produces simple upward boundary layer flow. In region I$b$ the buoyancy force distribution has only a weak outside reversal, and this is not strong enough to cause outside flow reversal.

As seen in figure 1, solutions were not obtained in region II, which includes a large portion of the $(t_\infty, s_\infty)$-plane. Solutions were obtained, however, at low salinities and high temperatures – regions III$a$ and III$b$. In these regions the downward thermal buoyancy is sufficiently strong to overcome the upward saline buoyancy close to the ice surface. In region III$a$, the saline buoyancy is dominant near the surface, while the downward thermal effect is stronger farther from the surface. The buoyancy force therefore reverses across the transport region. The upward saline buoyancy force is strongly damped by viscous forces near the wall. Hence, the weaker thermal buoyancy which acts farther from the surface dictates the dominant flow direction. In region III$b$ the saline buoyancy is so weak that the downward thermal buoyancy dominates all across the thermal transport region, resulting in a fully downward buoyancy force. The flow is then downward boundary-layer flow. The upper boundary to region III$a$ is the locus of $(t_\infty, s_\infty)$-conditions which result in $f''(0) = 0$. This zero-wall-shear condition marks the onset of inside flow reversal. The line between regions III$a$ and III$b$ is the locus of points where, as $s_\infty$ increases, a buoyancy-force reversal first occurs near the surface. The positions of these lines were interpolated from the computed results.

In figure 1, the boundaries of regions I$a$, I$b$, III$a$ and III$b$ intersect the $s_\infty = 0$ line at the values of $t_\infty$ indicated by the pure-water results of Carey *et al.* (1980). The computations provide no direct information about the flow behaviour in region II. However, the trends observed in the other regions can be extrapolated into region II. The expected flow behaviour in region II will be discussed after presenting the computed results in regions I and III.

Table 1 lists the computed interface conditions $t_0$ and $s_0$, and the corresponding transport parameters $A$, $B$, $Q$, $P$, $R$, $Pr$ and $Sc$ for the upward flows in regions I$a$ and I$b$. The additional computed transport quantities $f''(0)$, $\phi'(0)$, $S'(0)$, $f(0)$, $f(\infty)$ and $I_W$ are shown in table 2. For all calculations, the parameters $A$, $B$, $Q$, $P$, $R$ and $q$ were computed to seven significant figures to retain the full accuracy of the density relation. The resulting transport quantities and interface conditions were numerically determined to the number of digits listed in the tables. These quantities were calculated to high precision to minimize inaccuracies associated with the numerical scheme. It should be noted, however, that the accuracy of the results is limited by the assumptions used in the analysis (see § 2).

Also shown in table 2 is the calculated average melt rate for a 1 m long vertical ice surface for each of the ambient conditions listed there. The average melt rate for a surface of different length $L$, in metres, may be determined by multiplying the

| $t_\infty$ | $s_\infty$ | $t_0$ | $s_0$ | $-A\times100$ | $B\times100$ | $-Q$ | $-P$ | $R$ | $Pr$ | $Sc$ |
|---|---|---|---|---|---|---|---|---|---|---|
| 0 | 5 | −0·2677 | 4·598 | 0·03218821 | 0·1156753 | 0·3182985 | 426·5571 | −11·08784 | 13·25 | 2938 |
| 1 | 5 | −0·2095 | 3·452 | 0·1240212 | 0·4456976 | 0·2714653 | 94·36789 | −1·627518 | 12·99 | 2804 |
| 2 | 5 | −0·1679 | 2·629 | 0·1899807 | 0·6827370 | 0·2320075 | 47·84571 | −0·4467510 | 12·74 | 2680 |
| 3 | 5 | −0·1402 | 2·081 | 0·2339401 | 0·8407147 | 0·1972298 | 29·19547 | 0·01003031 | 12·50 | 2565 |
| 0 | 10 | −0·4795 | 8·719 | 0·1022902 | 0·3744675 | 0·5670764 | 455·9298 | −3·978765 | 13·31 | 2965 |
| 1 | 10 | −0·3818 | 6·827 | 0·2532371 | 0·9270591 | 0·4871300 | 151·9019 | −0·6568794 | 13·04 | 2825 |
| 2 | 10 | −0·3134 | 5·492 | 0·3598003 | 1·317169 | 0·4134144 | 81·29250 | 0·03990745 | 12·79 | 2697 |
| 2·5 | 10 | −0·2936 | 5·105 | 0·3907336 | 1·430410 | 0·3717828 | 61·75254 | 0·2120314 | 12·67 | 2637 |
| 0 | 15 | −0·6786 | 12·53 | 0·1966207 | 0·7333833 | 0·7732722 | 460·5558 | −1·248012 | 13·37 | 2992 |
| 1 | 15 | −0·5566 | 10·20 | 0·3814605 | 1·422824 | 0·6539711 | 185·2861 | 0·09838049 | 13·09 | 2847 |
| −1 | 20 | −1·062 | 19·68 | 0·02506418 | 0·09527208 | 1·091950 | 5635·897 | −12·78127 | 13·71 | 3183 |
| −0·5 | 20 | −0·9602 | 17·81 | 0·1733311 | 0·6588531 | 1·009118 | 860·1176 | −0·6215387 | 13·56 | 3098 |
| 0 | 20 | −0·8746 | 16·22 | 0·2994854 | 1·138381 | 0·9174134 | 440·1877 | 0·2446322 | 13·42 | 3018 |
| −1 | 22 | −1·145 | 21·21 | 0·06226374 | 0·2384827 | 1·153917 | 2780·294 | −2·497995 | 13·73 | 3195 |
| −1 | 24 | −1·227 | 22·72 | 0·1010566 | 0·3900419 | 1·194283 | 1929·819 | 0·2753471 | 13·75 | 3207 |
| −1 | 25 | −1·269 | 23·48 | 0·1202221 | 0·4657989 | 1·201872 | 1674·628 | 1·021260 | 13·76 | 3213 |
| −1 | 26 | −1·311 | 24·24 | 0·1386698 | 0·5393464 | 1·199113 | 1469·709 | 1·564184 | 13·77 | 3219 |
| −1† | 20 | −1·060 | 19·65 | 0·02733313 | 0·1038966 | 1·221710 | 6451·901 | −13·11305 | 13·71 | 3183 |
| −1† | 29 | −1·422 | 26·23 | 0·2175571 | 0·8560458 | 1·391099 | 1307·665 | 2·662165 | 13·80 | 3235 |
| −1† | 30 | −1·462 | 26·95 | 0·2395699 | 0·9463308 | 1·400068 | 1216·257 | 2·890372 | 13·81 | 3241 |
| −1† | 31 | −1·503 | 27·67 | 0·2610454 | 1·035185 | 1·403575 | 1133·509 | 3·079236 | 13·92 | 3247 |

TABLE 1. Interface conditions and transport parameters computed using the full analysis for $t_\infty$ and $s_\infty$ in regions I$a$ and I$b$ of figure 1. Also listed (†) are the results computed using the asymptotic analysis at the ambient conditions marked by open circles in figure 1.

| $t_\infty$ | $s_\infty$ | $t_0$ | $s_0$ | $f''(0)$ | $-\phi'(0)$ | $-S'(0)$ | $-f(0)\times10^3$ | $f(\infty)$ | $I_w$ | $\dot{M}$ (cm/day) |
|---|---|---|---|---|---|---|---|---|---|---|
| 0 | 5 | −0·2677 | 4·598 | 0·13397 | 0·64328 | 5·4914 | 0·054434 | 0·10700 | 0·14149 | 0·463 |
| 1 | 5 | −0·2095 | 3·452 | 0·14018 | 0·63407 | 4·6378 | 0·24714 | 0·10522 | 0·14741 | 2·91 |
| 2 | 5 | −0·1679 | 2·629 | 0·14510 | 0·61577 | 3·9101 | 0·43848 | 0·10061 | 0·15155 | 5·65 |
| 3 | 5 | −0·1402 | 2·081 | 0·14760 | 0·57815 | 3·3329 | 0·60763 | 0·088942 | 0·15231 | 8·17 |
| 0 | 10 | −0·4795 | 8·719 | 0·12322 | 0·56080 | 5·1044 | 0·084349 | 0·087914 | 0·12748 | 0·957 |
| 1 | 10 | −0·3818 | 6·827 | 0·12825 | 0·54612 | 4·4047 | 0·24151 | 0·084045 | 0·13206 | 3·40 |
| 2 | 10 | −0·3134 | 5·492 | 0·13177 | 0·51427 | 3·8251 | 0·38802 | 0·073850 | 0·13455 | 5·88 |
| 2·5 | 10 | −0·2936 | 5·105 | 0·13205 | 0·47708 | 3·6191 | 0·43871 | 0·059568 | 0·13380 | 6·73 |
| 0 | 15 | −0·6786 | 12·53 | 0·11879 | 0·50879 | 4·8870 | 0·10749 | 0·074754 | 0·12151 | 1·45 |
| 1 | 15 | −0·5566 | 10·20 | 0·12251 | 0·47777 | 4·2922 | 0·23636 | 0·064916 | 0·12444 | 3·71 |
| −1 | 20 | −1·062 | 19·68 | 0·11180 | 0·48303 | 5·3435 | 0·008999 | 0·068238 | 0·11389 | 0·0712 |
| −0·5 | 20 | −0·9602 | 17·81 | 0·11385 | 0·47183 | 5·0273 | 0·066478 | 0·064942 | 0·11570 | 0·877 |
| 0 | 20 | −0·8746 | 16·22 | 0·11545 | 0·45081 | 4·7339 | 0·12193 | 0·058097 | 0·11688 | 1·83 |
| −1 | 22 | −1·145 | 21·21 | 0·11103 | 0·46606 | 5·2635 | 0·020388 | 0·063598 | 0·11276 | 0·221 |
| −1 | 24 | −1·227 | 22·72 | 0·11011 | 0·44335 | 5·1863 | 0·030377 | 0·057001 | 0·11143 | 0·361 |
| −1 | 25 | −1·269 | 23·48 | 0·10956 | 0·42838 | 5·1484 | 0·034680 | 0·052453 | 0·11065 | 0·427 |
| −1 | 26 | −1·311 | 24·24 | 0·10902 | 0·41091 | 5·1135 | 0·038436 | 0·046631 | 0·10986 | 0·488 |
| −1† | 20 | −1·060 | 19·65 | 0·1123 | 0·5424 | 5·356 | 0·00985 | — | 0·1123 | 0·0823 |
| −1† | 29 | −1·422 | 26·23 | 0·1088 | 0·4325 | 5·025 | 0·05461 | — | 0·1088 | 0·767 |
| −1† | 30 | −1·462 | 26·95 | 0·1083 | 0·4209 | 4·995 | 0·05813 | — | 0·1083 | 0·837 |
| −1† | 31 | −1·503 | 27·67 | 0·1079 | 0·4083 | 4·963 | 0·06126 | — | 0·1079 | 0·897 |

TABLE 2. Interface conditions and transport quantities computed using the full analysis for $t_\infty$ and $s_\infty$ in regions I$a$ and I$b$ of figure 1. Also listed (†) are the results computed using the asymptotic analysis at the ambient conditions marked by open circles in figure 1. For each circumstance, the average melt rate $\dot{M}$ is listed for a 1 m long vertical ice surface.

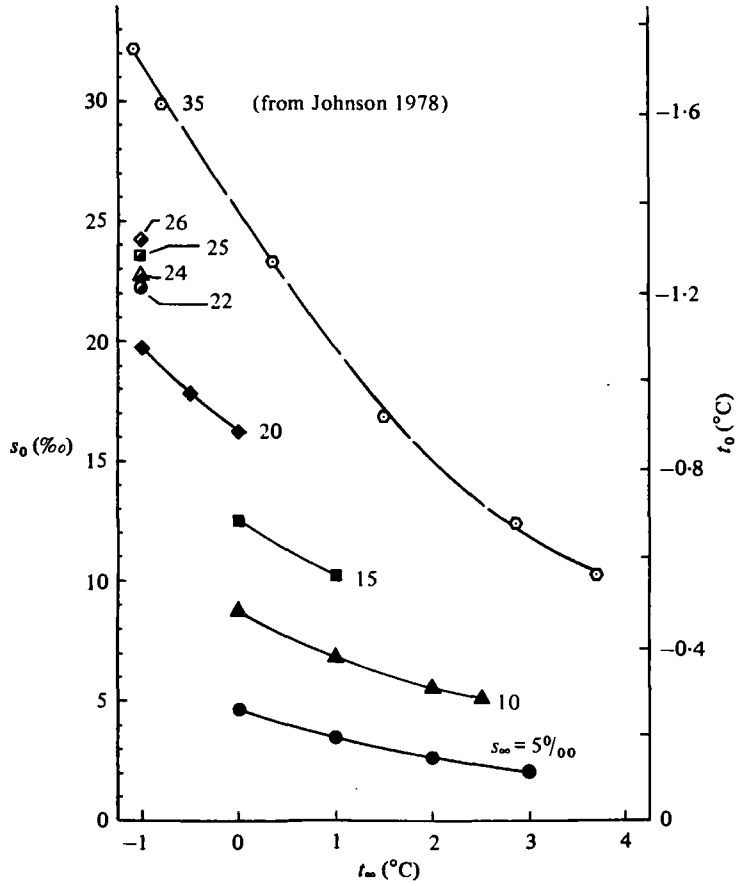


FIGURE 2. Computed interface conditions for $t_\infty < 5$ °C. ●, $s_\infty = 5‰$; ▲, 10; ■, 15; ◆, 20; ◕, 22; ◭, 24; ◪, 25; ◈, 26. Also shown (⊙) are the measured interface conditions of Johnson (1978) for $s_\infty = 35‰$.

listed value by $L^{-\frac{1}{4}}$. It can be seen that for $s_\infty$ fixed, increasing $t_\infty$ increases the melt rate as expected. Also, as $s_\infty$ increases with $t_\infty$ fixed, the melt rate also increases.

The computed values of $t_0$ and $s_0$ within regions I$a$ and I$b$ are seen in figure 2. Recall that $t_0 = t_{11}(s_0)$. For fixed $s_\infty \leqslant 20‰$, increasing $t_\infty$ is seen to decrease $s_0$ and increase $t_0$. Also shown in figure 2 are the measured interface conditions of Johnson (1978) for $s_\infty = 35‰$ and $t_\infty$ between $-1{\cdot}05$ °C and 4·0 °C. For these ambient conditions, which lie in region II of figure 1, the measured surface temperatures show the same trend as the computed results in regions I$a$ and I$b$, with $t_0$ increasing as $t_\infty$ is increased with $s_\infty$ fixed. Figure 3 shows the heat- and mass-transfer parameters $-\phi'(0)$ and $S'(0)$, for $t_\infty$ and $s_\infty$ in regions I$a$ and I$b$. It is seen that at all ambient salinity levels, increasing $t_\infty$ results in both lower $-\phi'(0)$ and $-S'(0)$. At fixed $t_\infty$, decreasing $s_\infty$ increases $-\phi'(0)$ and $-S'(0)$. In region I, as ambient conditions are further removed from the $t_m(s_\infty)$ line, the thermal buoyancy becomes stronger. This increases the thermal and saline transport.

For the downward flows in regions III$a$ and III$b$, the transport parameters and computed interface conditions are listed in tables 3 and 4. Also shown are the corre-

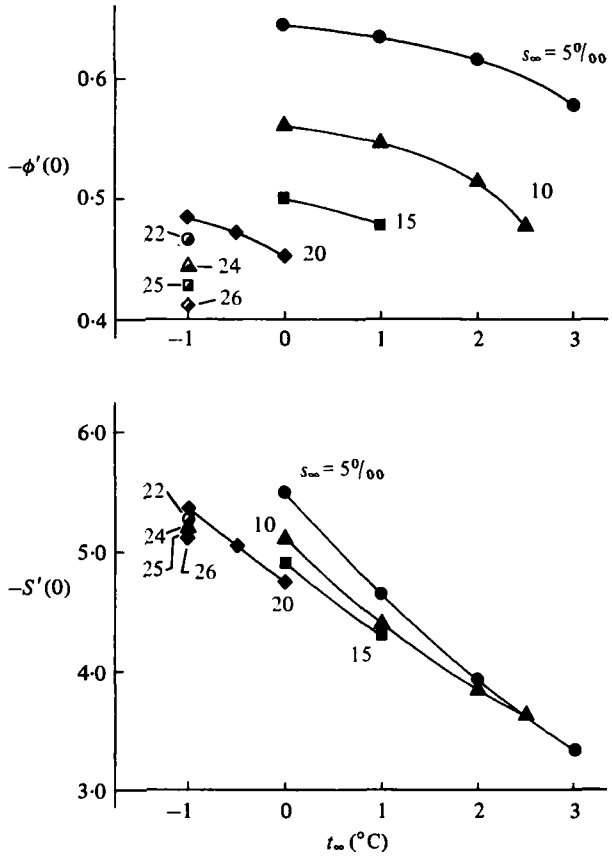


FIGURE 3. Computed transport quantities for $t_\infty < 5$ °C.
●, $s_\infty = 5‰$; ▲, 10; ■, 15; ◆, 20; ◕, 22; ◬, 24; ◪, 25; ◈, 26.

| $t_\infty$ | $s_\infty$ | $t_0$ | $s_0$ | $-A\times100$ | $B\times100$ | $-Q$ | $-P$ | $R$ | $Pr$ | $Sc$ |
|---|---|---|---|---|---|---|---|---|---|---|
| 10 | 1 | −0·000410 | 0·00603 | 0·07991228 | 0·2830014 | 0·02108769 | 1·098114 | 0·6182586 | 10·99 | 1925 |
| 10 | 1·06 | −0·000164 | 0·00241 | 0·08502277 | 0·3011657 | 0·02243791 | 1·168593 | 0·6195468 | 10·99 | 1925 |
| 15 | 1 | −0·000161 | 0·00237 | 0·08020629 | 0·2840426 | 0·01411061 | 0·5112188 | 0·7455146 | 10·10 | 1607 |
| 15 | 2 | −0·000203 | 0·00298 | 0·1604248 | 0·5702092 | 0·02824601 | 1·025430 | 0·7596566 | 10·10 | 1607 |
| 15 | 2·835 | −0·000054 | 0·00079 | 0·2275255 | 0·8111861 | 0·04008769 | 0·457838 | 0·7714766 | 10·10 | 1607 |
| 20 | 1 | −0·000036 | 0·00052 | 0·08035493 | 0·2845690 | 0·01060266 | 0·2969493 | 0·8091405 | 9·312 | 1361 |
| 20 | 2 | −0·000057 | 0·00084 | 0·1605972 | 0·5708218 | 0·02120749 | 0·5951761 | 0·8197479 | 9·315 | 1361 |
| 20 | 3 | −0·000064 | 0·00094 | 0·2407276 | 0·8587741 | 0·03181455 | 0·8946947 | 0·8303558 | 9·319 | 1361 |
| 20 | 4 | −0·000054 | 0·00079 | 0·3207501 | 1·148454 | 0·04242436 | 1·195532 | 0·8409644 | 9·322 | 1361 |
| 20 | 5 | −0·000018 | 0·00022 | 0·4006748 | 1·439912 | 0·05303829 | 1·497742 | 0·8515741 | 9·326 | 1361 |
| 20 | 5·082 | −0·000011 | 0·00016 | 0·4072277 | 1·463903 | 0·05390928 | 1·522598 | 0·8524443 | 9·326 | 1361 |

TABLE 3. Interface conditions and transport parameters for $t_\infty$ and $s_\infty$ in regions III$a$ and III$b$ of figure 1.

sponding average melt rates for a vertical ice surface 1 m long. It is seen that melt rates at the high ambient temperatures in regions III$a$ and III$b$ are much higher than those in regions I$a$ and I$b$. Increasing $s_\infty$ with $t_\infty$ fixed decreases the melt rate because the resulting increase in saline buoyancy opposes the thermal buoyancy which dominates the flow. In regions III$a$ and III$b$, the interface conditions $t_0$ and $s_0$ are seen to be

| $t_\infty$ | $s_\infty$ | $t_0$ | $s_0$ | $f''(0)$ | $-\phi'(0)$ | $-S'(0)\times 10^3$ | $-f(0)\times 100$ | $f(\infty)$ | $-I_W$ | $\dot{M}$ (cm/day) |
|---|---|---|---|---|---|---|---|---|---|---|
| 10 | 1 | −0·000410 | 0·00603 | 0·036213 | 0·92529 | 123·71 | 0·35289 | 0·23445 | 0·10249 | 32·9 |
| 10 | 1·06 | −0·000164 | 0·00241 | −0·031201 | 0·86089 | 43·211 | 0·32832 | 0·23191 | 0·036535 | 30·7 |
| 15 | 1 | −0·000161 | 0·00237 | 0·26932 | 1·0303 | 73·393 | 0·64068 | 0·25879 | 0·73021 | 70·1 |
| 15 | 2 | −0·000203 | 0·00298 | 0·16470 | 0·98841 | 44·218 | 0·61403 | 0·25742 | 0·26001 | 67·2 |
| 15 | 2·835 | −0·000054 | 0·00079 | −0·0046114 | 0·87711 | 7·3332 | 0·54488 | 0·25264 | 0·062605 | 59·6 |
| 20 | 1 | −0·000036 | 0·00052 | 0·35328 | 1·0213 | 19·552 | 0·91747 | 0·27254 | 1·6020 | 112·0 |
| 20 | 2 | −0·000057 | 0·00084 | 0·29658 | 1·0027 | 15·409 | 0·90048 | 0·27196 | 0·70210 | 109·0 |
| 20 | 3 | −0·000064 | 0·00094 | 0·23272 | 0·97906 | 11·277 | 0·87786 | 0·27108 | 0·39393 | 107·0 |
| 20 | 4 | −0·000054 | 0·00079 | 0·15581 | 0·94507 | 6·8503 | 0·84652 | 0·26965 | 0·22853 | 103·0 |
| 20 | 5 | −0·000018 | 0·00022 | 0·031742 | 0·86757 | 1·7147 | 0·77614 | 0·26590 | 0·095956 | 94·9 |
| 20 | 5·082 | −0·000011 | 0·00016 | −0·00003166 | 0·83874 | 0·91413 | 0·75035 | 0·26442 | 0·072229 | 91·6 |

TABLE 4. Interface conditions and transport quantities for $t_\infty$ and $s_\infty$ in regions III$a$ and III$b$ of figure 1. Also shown are the corresponding average melt rates $\dot{M}$ for a 1 m long vertical ice surface.

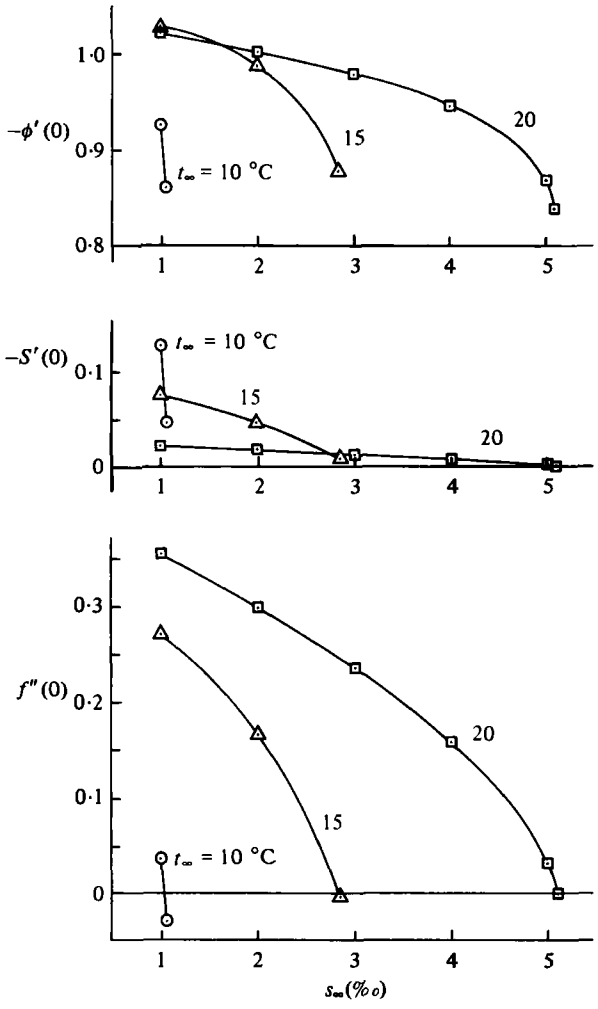


FIGURE 4. Computed transport quantities for $t_\infty > 5$ °C.
⊙, $t_\infty = 10$ °C; △, 15; ⊡, 20.

virtually zero for all ambient conditions. This results from the very rapid rate of fresh-water melt addition which occurs in such warm ambient conditions. In figure 4, $\phi'(0)$, $S'(0)$ and $f''(0)$ are plotted for $s_\infty$ at $t_\infty = 10$, 15 and 20 °C. At each $t_\infty$, it can be seen that increasing $s_\infty$ decreases the heat and mass transfer at the surface, with the effect being stronger at lower $t_\infty$. Increasing $s_\infty$ with $t_\infty$ fixed is also seen to reduce $f''(0)$. Sufficiently large $s_\infty$ results in $f''(0) < 0$, implying a small region of upward flow near the surface.

Figures 5–7 show the effect of changing $s_\infty$ with $t_\infty$ fixed for calculations in regions I*a* and I*b*. Figure 5 shows the velocity profiles for $s_\infty = 20$, 22, 24 and 26‰ with $t_\infty$ fixed at $-1$ °C (cf. figure 1). The corresponding $\phi(\eta)$ and $S(\eta)$ profiles are shown in figure 6, and the buoyancy-force profiles $W(\eta)$ are shown in figure 7. For $t_\infty = -1$, the buoyancy force is completely upward for $s_\infty = 20$ and 22‰. For $s_\infty = 24$ and 26‰, $W$ is positive near the surface and very weakly negative near the outer edge

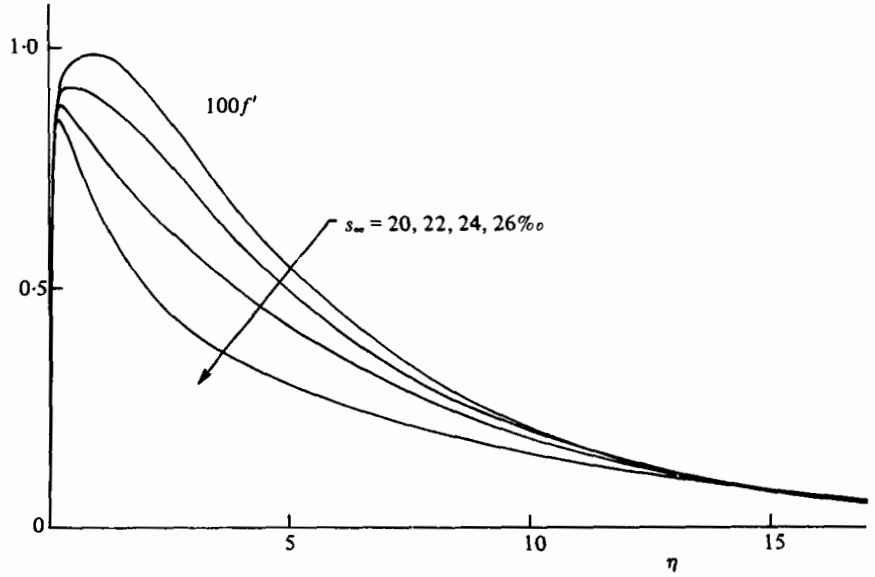


FIGURE 5. Velocity profiles for $t_\infty = -1$ °C; $s_\infty = 20, 22, 24, 26$‰.

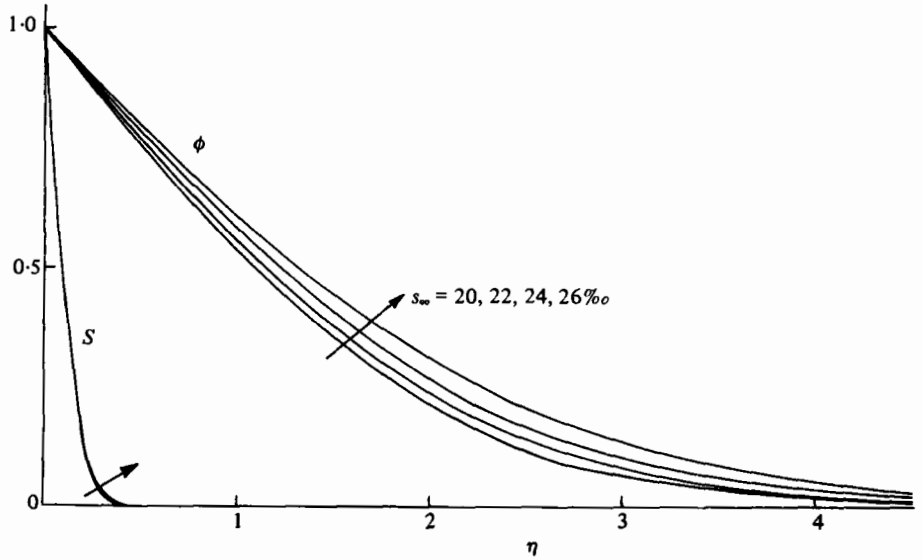


FIGURE 6. Temperature and salinity profiles for $t_\infty = -1$ °C; $s_\infty = 20, 22, 24, 26$‰.

of the thermal layer. Yet the very small change in the buoyancy force distribution seen in figure 7 has the strong effect on the velocity profile seen in figure 5. The weak downward buoyancy force produces a large velocity reduction over almost the entire boundary layer. In figure 6, the temperature profile is also strongly affected. The salinity distribution shows only a very small change.

Figures 8–10 also relate to region I. However, the effects of changing $t_\infty$ at a given level of $s_\infty$ are seen. Figure 8 shows decreasing velocity as $t_\infty$ increases at $s_\infty = 10$‰. The corresponding $\phi$ and $S$ profiles are shown in figure 9, and $W(\eta)$, the buoyancy-force distribution, is shown in figure 10. As $t_\infty$ increases, the buoyancy force near

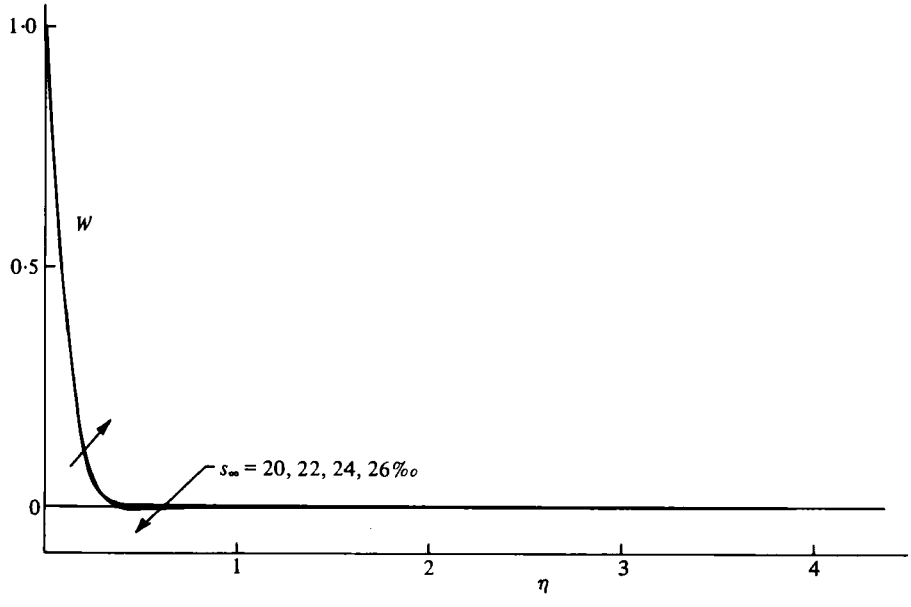


FIGURE 7. Buoyancy-force distributions for $t_\infty = -1$ °C; $s_\infty$ = 20, 22, 24, 26‰.

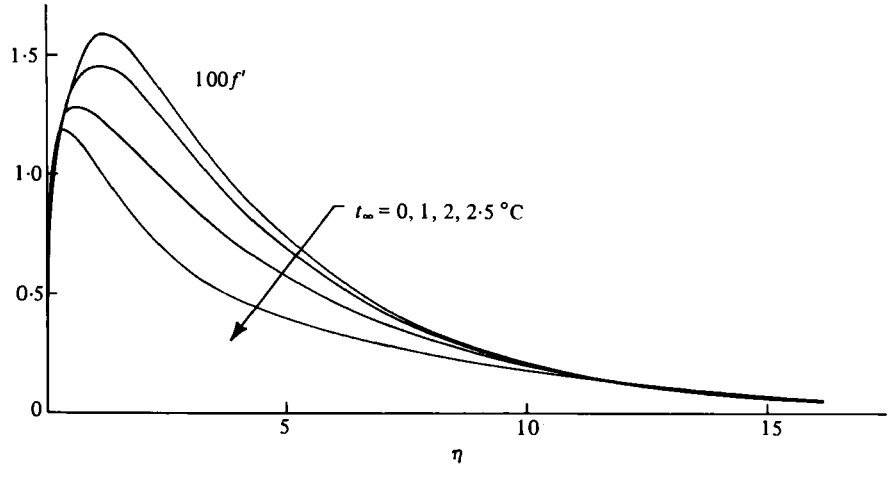


FIGURE 8. Velocity profiles for $s_\infty$ = 10‰; $t_\infty$ = 0, 1, 2, 2·5 °C.

$\eta = 1{\cdot}5$ decreases, becoming slightly negative for $t_\infty = 2{\cdot}0$ and 2·5 °C. This reduces the velocity, as seen in figure 8. Significant changes in $\phi(\eta)$ are also seen in figure 9. $S(\eta)$ is also affected, but to a lesser extent.

Figures 11–13 show typical $f'$, $\phi$, $S$ and $W$ profiles for the downward flows found in regions III$a$ and III$b$ of figure 1. For $t_\infty = 15$ °C, figure 11 indicates that in region III, changing $s_\infty$ has only a slight effect on the velocity profiles. For $(t_\infty, s_\infty) = (15, 2{\cdot}835)$ a small local flow reversal near the surface is indicated in table 4, since $f''(0)$ is negative. However, figure 11 indicates that this reversal is extremely small. Comparing the results at (10, 1) and (15, 1), it is seen that changing $t_\infty$ also has a weak effect on the velocity profiles. In contrast, changing $s_\infty$ or $t_\infty$ significantly alters the $\phi$ and $S$ profiles, as seen in figure 12. This, in turn, changes the buoyancy-force distribution in figure 13.

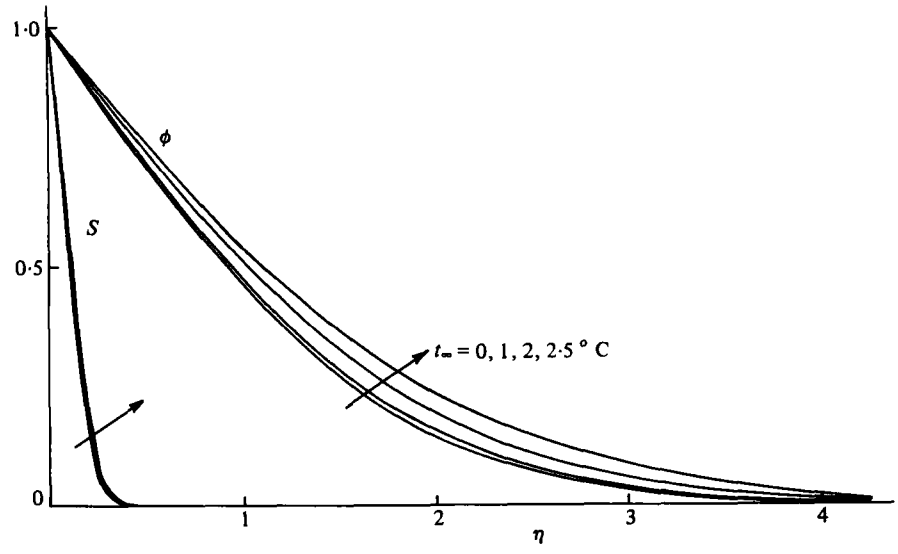


FIGURE 9. Temperature and salinity profiles for $s_\infty = 10\,‰$; $t_\infty = 0$, 1, 2, 2·5 °C.

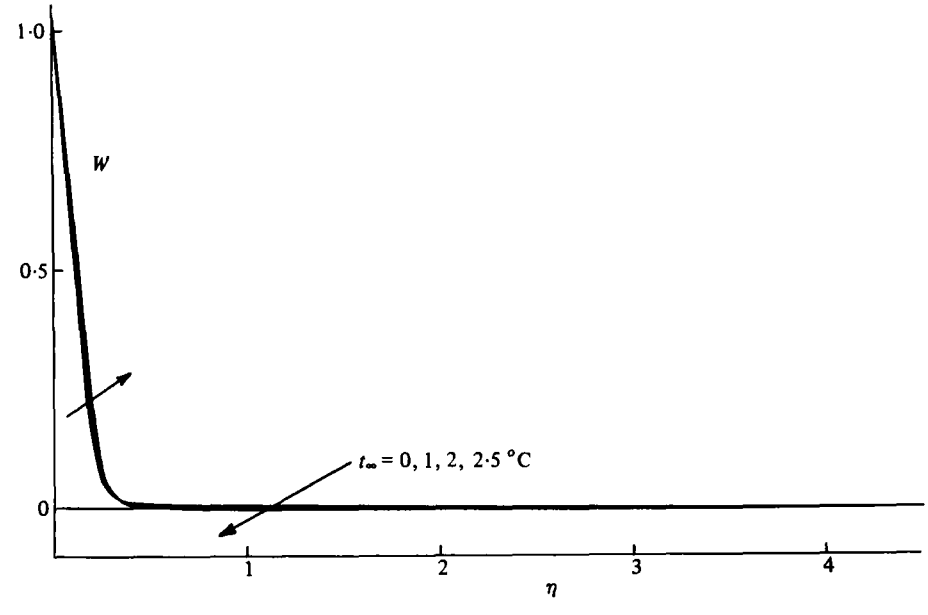


FIGURE 10. Buoyancy-force distributions for $s_\infty = 10\,‰$; $t_\infty = 0$, 1, 2, 2·5 °C.

The buoyancy force for these circumstances is strongly bi-directional. Note that the slope of $S(\eta)$ near $\eta = 0$ is almost zero. At these ambient-temperature levels, fresh water is generated so rapidly by melting that little salinity is transported by molecular diffusion to the surface. The interface motion is so rapid that a sizable region exists near the ice surface where the salinity gradient is small and the local salinity is almost zero. This effect would be completely missed in calculations with a fixed co-ordinate system that neglected the motion of the interface.

Numerical convergence could not be obtained for $s_\infty$ greater than 26 ‰, even at very

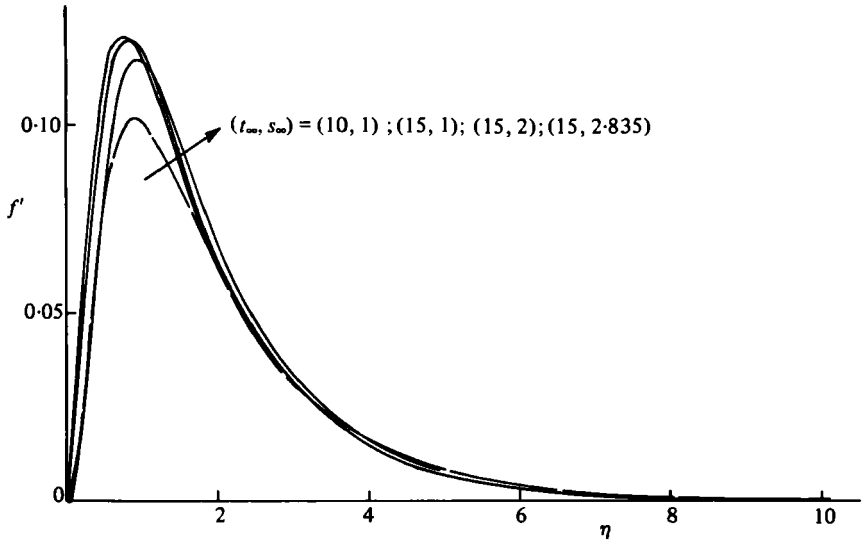


FIGURE 11. Velocity profiles for $(t_\infty, s_\infty)$ = (10, 1), (15, 1), (15, 2), (15, 2·835).

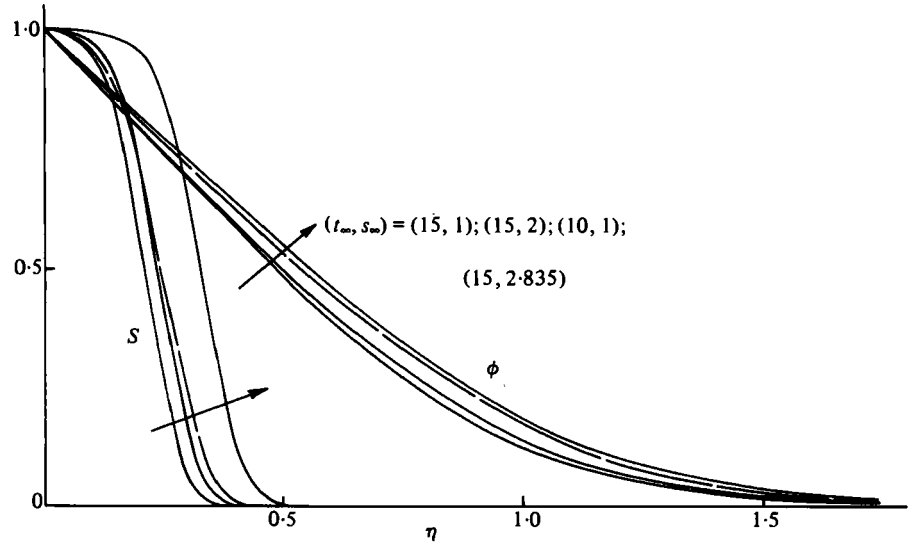


FIGURE 12. Temperature and salinity profiles for $(t_\infty, s_\infty)$ = (10, 1), (15, 1), (15, 2), (15, 2·835).

low values of $t_\infty$ (cf. figure 1). This is unfortunate since low values of $t_\infty$ with $s_\infty$ near 35‰ are conditions which commonly arise for sea ice. The outside buoyancy-force reversals which are believed to arise for these circumstances would tend to cause appreciable outside flow reversal. Even the smallest outside flow reversal causes the numerical scheme to become unstable. To circumvent this difficulty, at low temperatures and high salinities, a slightly modified form of the analysis of Stewartson & Jones (1957) was used. They point out that for high Prandtl number flows driven by thermal buoyancy alone, with the Boussinesq approximation of $\rho_\infty - \rho$, the boundary region consists of two parts. The inner region is dominated by a balance between

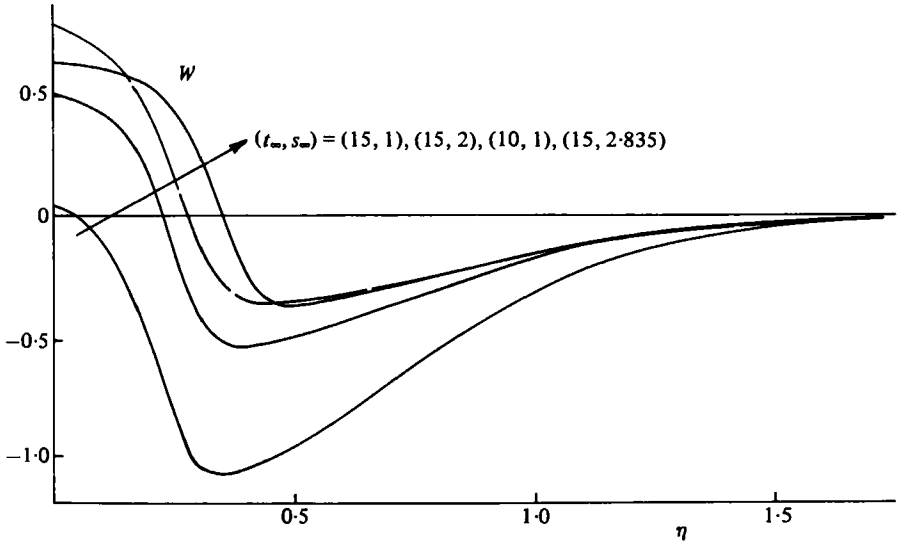


FIGURE 13. Buoyancy-force distributions for $(t_\infty, s_\infty) = (10, 1), (15, 1), (15, 2), (15, 2{\cdot}835)$.

viscous and buoyancy forces, and, to first order, is independent of the outer flow behaviour. Outside this inner thermal region, the flow is governed by a balance between inertial and viscous forces. A solution was obtained for the inner region, valid for large $Pr$, that is independent of the outer flow behaviour. These inner solutions are actually the lowest-order terms in the inner series of a matched asymptotic expansion solution of the governing equations.

Following Stewartson & Jones (1957), new variables $F$, $\overline{\phi}$, $\overline{S}$ and $\zeta$ are defined as

$$F(\zeta) = (3Pr)^{\frac{1}{3}} f(\eta), \quad \zeta = (3Pr)^{\frac{1}{3}} \eta; \tag{31}$$

$$\overline{\phi}(\zeta) = \phi(\eta), \quad \overline{S}(\zeta) = S(\eta). \tag{32}$$

$F$, $\overline{\phi}$, $\overline{S}$ and $\zeta$ are substituted into (23) and (26) with (24$a$). Then, letting $Pr \to \infty$ and $Sc \to \infty$ such that $Le = Sc/Pr$ is constant, the equations and boundary conditions for the inner region become

$$F''' + \overline{S} + \frac{1}{P}\{|R|^a - (1+A\overline{S})(1+B\overline{S})|\overline{\phi} - R - QS|^a\} = 0; \tag{33$a$}$$

$$\overline{\phi}'' + F\overline{\phi}' = 0; \tag{33$b$}$$

$$\overline{S}'' + LeF\overline{S}' = 0; \tag{33$c$}$$

$$F(0) = \frac{-\overline{\phi}'(0)\, c_p(t_0 - t_\infty)}{h_{11}(1 - 10^{-3}s_0)}, \quad F'(0) = 0, \quad \overline{\phi}(0) = 1, \quad \overline{S}(0) = 1; \tag{34$a$}$$

$$F''(\infty) = 0, \quad \overline{\phi}(\infty) = 0, \quad \overline{S}(\infty) = 0. \tag{34$b$}$$

The added condition (27) becomes

$$\frac{\overline{S}'(0)}{\overline{\phi}'(0)} - Le\frac{c_p(t_0 - t_\infty)}{h_{11}} \frac{s_0}{(1 - 10^{-3}s_0)(s_0 - s_\infty)} = 0. \tag{35}$$

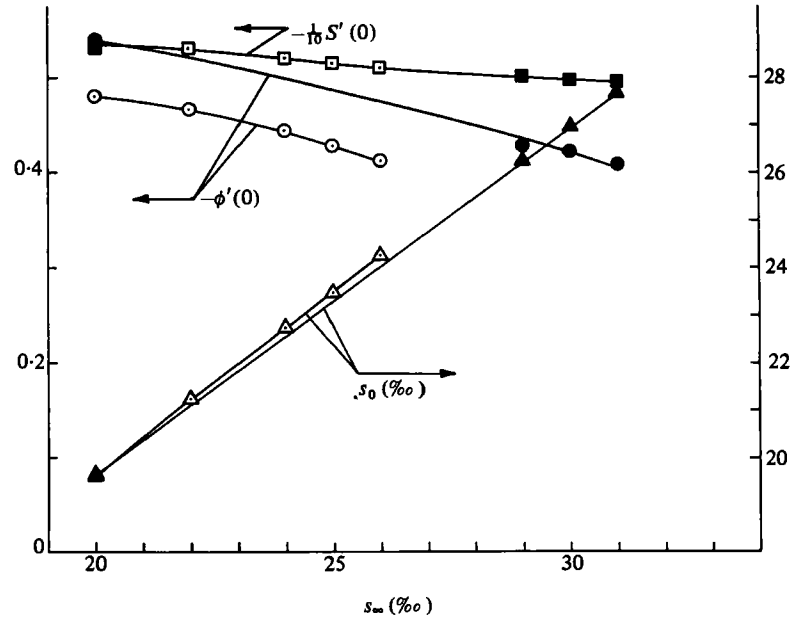


FIGURE 14. Transport quantities and interface salinity computed by the full analysis (open symbols) and the asymptotic analysis (filled symbols) for $t_\infty = -1$ °C.

The solution for this inner region determines the surface-transport and interface conditions, independent of the outer flow behaviour. In the outer region, $S$ and $\phi$ are exponentially small and are neglected to a first approximation. The flow in the outer region can then be determined by rescaling $f$ and $\eta$ and matching $f'$ at the outer edge of the thermal region with $f'$ at the inner edge of the outer region. Details of the procedure are described by Stewartson & Jones (1957). The solution in the outer region was not determined here because the objective was only to obtain approximations for the interface conditions and transport quantities.

Equations (33) with boundary conditions (34) were integrated in the same manner as the full equations, using (35) to determine iteratively the interface conditions $t_0$ and $s_0$. Since the asymptotic analysis is an approximation of the full solution as $Pr \to \infty$ and $Sc \to \infty$, the interface conditions and transport quantities were determined numerically only to four significant figures. The results of the integration of (33) with (34) and (35) are listed in tables 1 and 2 for the ambient conditions marked by open circles in figure 1. The results of the asymptotic analysis were converted to the original similarity variables using (31) and (32) with the value of $Pr$ at $t_f$ and $s_f$.

In figure 14, the computed values of $s_0$, $-\phi'(0)$ and $-S'(0)$ are plotted for different $s_\infty$ at $t_\infty = -1$ °C. The results of the full solution and the asymptotic solution are shown. The asymptotic solution was computed for $(t_\infty, s_\infty) = (-1, 20)$ to compare the asymptotic results with the full analysis. As seen in figure 14 and table 2, the asymptotic solution and the full solution predict almost identical values and trends of $S'(0)$ and $s_0$. However, the values of $\phi'(0)$ differ by about 10 %. The value of $Pr$ is only about 13. The error in $\phi'(0)$ may therefore be largely due to inaccuracy associated with the assumption of $Pr \to \infty$. Since $Sc$ is about 3000, the large-$Sc$ approximation is much better. This may account for the better agreement with $S'(0)$ from the full solution.

As seen in figure 14, use of the asymptotic analysis permits calculation of the transport and interface conditions to salinities as high as 31 ‰. Beyond 31 ‰ numerical instability again made computations impossible. The asymptotic analysis can also be used at lower salinities to predict transport and interface conditions further into region II than is possible with the full analysis. However, even then, only limited penetration is possible.

## 5. Conclusions

The present analysis predicts the surface conditions, transport and flow behaviour near a vertical ice surface melting in saline water for $(t_\infty, s_\infty)$ in regions I*a*, I*b*, III*a* and III*b* of figure 1. By means of an asymptotic analysis valid for large $Pr$ and $Sc$, the calculations have been extended farther into region II for low $t_\infty$. The only previous experimental data available for these conditions are the measured interface conditions of Josberger & Martin (1981). For $(t_\infty, s_\infty) = (0{\cdot}05, 14{\cdot}2)$ and $(1{\cdot}80, 8{\cdot}0)$ they found $t_0 = -0{\cdot}66$ and $-0{\cdot}29$ °C respectively. Solutions have not been computed for these particular conditions, but linear interpolation of the computed results predicts $t_0 = -0{\cdot}64$ and $-0{\cdot}29$ °C respectively for $(t_\infty, s_\infty) = (0{\cdot}05, 14{\cdot}2)$ and $(1{\cdot}80, 8{\cdot}0)$. The computed results are therefore in excellent agreement with the measurements of Josberger & Martin (1981).

Few computed solutions were obtained in the very large region II in figure 1. The use of the asymptotic analysis extended the calculations only slightly into region II. However, the results in regions I*b* and III*a* provide some insight as to possible flow behaviour in region II. As ambient conditions become progressively closer to the boundary of region II, the buoyancy force computed in regions I*b* and III*a* becomes more strongly bi-directional. In region III*a* this leads to a small region of reversed flow near the surface. If this observed trend continues into region II, it is expected that the flow in at least part of region II is laminar and bi-directional. None of the computed results in region I*b* indicate bi-directional flow. However, the trend in the buoyancy force suggests that outside flow reversal is likely to occur at slightly higher $t_\infty$ or $s_\infty$. Hence, the upper boundary of region I*b* in figure 1 is tentatively placed just beyond the limits of these calculations. The strong buoyancy at higher temperatures and salinities may result in turbulent flows. Both bi-directional laminar flow and turbulent flow were observed by Josberger & Martin (1981) at $s_\infty \simeq 33$ ‰. The calculations presented here suggest that flows of these types may occur at lower salinities in region II.

Slightly beyond the upper boundaries of regions I*b* and III*a*, the numerical calculation scheme failed to converge. The trends in the computed results suggest that this breakdown of the computational scheme is associated with a transition from laminar boundary-layer flow to some other mode of transport, possibly one of the modes discussed above. Knowledge of the conditions at which such transitions occur is essential to predict accurately the transport near melting ice masses. The transitions to non-boundary-layer flow indicated by the present analysis are in agreement with the limited experimental observations of Johnson (1978) and Josberger & Martin (1981)

Comparison of the analytical results with new experimental data in regions I*a*, I*b* and II will be made in a companion paper: Carey & Gebhart (1982). This new experimental data, together with the present calculations and the experimental results of

Josberger & Martin (1981) and Johnson (1978) will provide, for the first time, a full picture of the flow behaviour in the entire $(t_\infty, s_\infty)$-plane in figure 1.

The first author wishes to acknowledge graduate-fellowship support from the Graduate School at the State University of New York at Buffalo. The authors also wish to acknowledge support for this study by the National Science Foundation under research grant ENG77-21641.

## REFERENCES

Carey, V. P. 1981 Transport in vertical mixed convection flows and natural convection flows in cold water. Ph.D. thesis, State University of New York at Buffalo.

Carey, V. P. & Gebhart, B. 1981 Visualization of the flow adjacent to a vertical ice surface melting in cold pure water. *J. Fluid Mech.* **107**, 37–55.

Carey, V. P. & Gebhart, B. 1982 Transport near a vertical ice surface melting in saline water: experiments at low salinities. *J. Fluid Mech.* **117**, 403–423.

Carey, V. P., Gebhart, B. & Mollendorf, J. C. 1980 Buoyancy force reversals in vertical natural convection flows in cold water. *J. Fluid Mech.* **97**, 279–297.

Fujino, K., Lewis, E. L. & Perkin, R. G. 1974 The freezing point of sea water at pressures up to 1000 bars. *J. Geophys. Res.* **79**, 1792–1797.

Gebhart, B. & Mollendorf, J. C. 1977 A new density relation for pure and saline water. *Deep-Sea Res.* **24**, 831–848.

Gebhart, B. & Mollendorf, J. C. 1978 Buoyancy-induced flows in water under conditions in which density extrema may arise. *J. Fluid Mech.* **89**, 673–707.

Huppert, H. E. & Turner, J. S. 1978 On melting icebergs. *Nature* **271**, 46–48.

Johnson, R. S. 1978 Transport from a melting vertical ice slab in saline water. M.S. thesis, State University of New York at Buffalo.

Josberger, E. G. 1979 Laminar and turbulent boundary layers adjacent to melting vertical ice walls in salt water. *Scientific Rep.* no. 16, *Office of Naval Research.*

Josberger, E. G. & Martin, S. 1981 A laboratory and theoretical study of the boundary layer adjacent to a vertical melting ice wall in salt water. *J. Fluid Mech.* **111**, 439–473.

Marschall, E. 1977 Free convection melting on glacial ice in saline water. *Lett. Heat Mass Transfer* **4**, 381–384.

Mollendorf, J. C., Kukulka, D. & Gebhart, B. 1982 Transport properties of seawater (in preparation).

Neshyba, S. & Josberger, E. G. 1980 On the estimation of antarctic iceberg melt rate. *J. Phys. Oceanog.* **10**, 1681–1685.

Stewartson, K. & Jones, L. T. 1957 The heated vertical plate at high Prandtl number. *J. Aero. Sci.* **24**, 379–380.

Vanier, C. R. & Tien, C. 1968 Effect of maximum density and melting on natural convection heat transfer from a vertical plate. *Chem. Engng Prog. Symp. Series* **64**, 240–254.

Wilson, N. W. & Vyas, B. D. 1979 Velocity profiles near a vertical ice surface melting into fresh water. *Trans. A.S.M.E.* C, *J. Heat Transfer* **101**, 313–317.